Biomedical Physics & Engineering Express

ENDORSED BY IPEM Institute of Physics and Engineering in Medicine

PAPER • OPEN ACCESS

Light-based 3D printing of hydrogels with high-resolution channels

To cite this article: Aaron D Benjamin *et al* 2019 *Biomed. Phys. Eng. Express* **5** 025035

Biomedical Physics & Engineering Express

PAPER

Light-based 3D printing of hydrogels with high-resolution channels

Aaron D Benjamin[1,3,5], **Reha Abbasi**[1,2,5], **Madison Owens**[1,2], **Robert J Olsen**[1,2], **Danica J Walsh**[1,4], **Thomas B LeFevre**[1,2] and **James N Wilking**[1,2,5]

[1] Center for Biofilm Engineering, Montana State University, 366 Barnard Hall, Bozeman, MT, 59717, United States of America
[2] Chemical and Biological Engineering Department, Montana State University, 306 Cobleigh Hall, Bozeman, MT, 59717, United States of America
[3] Mechanical and Industrial Engineering Department, Montana State University, 220 Roberts Hall, Bozeman, MT, 59717, United States of America
[4] Department of Chemistry and Biochemistry, Montana State University, 103 Chemistry and Biochemistry, Bozeman, MT, 59717, United States of America
[5] Co-first author.

E-mail: james.wilking@montana.edu

Keywords: 3D printing, additive manufacturing, SLA, stereolithography, hydrogel, vasculature, photopolymerization

Supplementary material for this article is available online

OPEN ACCESS

RECEIVED
20 June 2018

REVISED
12 July 2018

ACCEPTED FOR PUBLICATION
27 July 2018

PUBLISHED
28 January 2019

Abstract

Hydrogels are soft, water-based gels with widespread applications in personal care products, medicine and biomedical engineering. Many applications require structuring the hydrogel into complex three-dimensional (3D) shapes. For these applications, light-based 3D printing methods offer exquisite control over material structure. However, the use of these methods for structuring hydrogels is underdeveloped. In particular, the ability to print hydrogel objects containing internal voids and channels is limited by the lack of well-characterized formulations that strongly attenuate light and the lack of a theoretical framework for predicting and mitigating channel occlusion. Here we present a combined experimental and theoretical approach for creating well-defined channels with any orientation in hydrogels using light-based 3D printing. This is achieved by the incorporation of photoblocker and the optimization of print conditions to ensure layer-layer adhesion while minimizing channel occlusion. To demonstrate the value of this approach we print hydrogels containing individual spiral channels with centimeter-scale length and submillimeter-scale cross-section. While the channels presented here are relatively simple, this same approach could be used to achieve more complex channel designs mimicking, for example, the complex vasculature of living organisms. The low cytotoxicity of the gel makes the formulation a promising candidate for biological applications.

Introduction

Hydrogels are water-based gels comprised of polymer dissolved in water and crosslinked to form a solid [1–3]. Typically, hydrogels contain a low mass fraction of polymer; thus, they are soft and easily deformed. In addition, many hydrogels are compatible with biological systems [4] and have widespread applications in personal care products [5], medicine [6–9], and bioengineering [10, 11]. For many applications, the ability to form soft hydrogel into complex, three-dimensional structures is critical. For example, when hydrogel is used as a tissue scaffold [12] internal channels with high permeability to liquid flow must be incorporated to mimic tissue vasculature and maintain cell viability [13–16]. Likewise, in microfabrication, the ability to control hydrogel structure with high fidelity is important [17–19]. Applications such as these require methods and technologies for accurately and precisely building hydrogel objects with complex, sub-millimeter-scale structures.

Three-dimensional (3D) printing technologies provide exquisite control over material structure [20]. For example, in fused deposition modeling (FDM) printing, a three-dimensional object is built layer-by-layer by extruding thermoplastic from a nozzle, which is translated in the *xy*-plane. Modified versions of these extrusion-based printers have been used to print hydrogels [21, 22] but are limited by their resolution

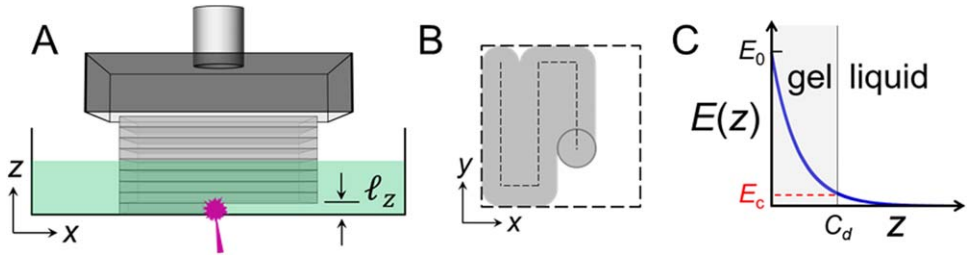

Figure 1. *Light-based stereolithographic 3D printing.* (**A**) Illustration of a stereolithography (SLA)-based 3D printer used to print hydrogel. An object is printed layer-by-layer by polymerization of a liquid resin (green) to a solid upon exposure to laser light (violet). Layer thickness, ℓ_z is set by the gap between the underside of the object and the bottom surface of the resin tray. (**B**) A single layer in the *xy* plane is formed by raster-scanning a focused laser light spot (circle) within the plane. (**C**) Light is attenuated by the liquid resin, and light exposure, $E(z)$ decreases with depth, z. At a critical exposure value, E_c, the light is insufficient to induce polymerization and this defines the cure depth, C_d beyond which resin remains liquid.

and speed. By contrast, light-based 3D printing methods can be used to form objects much faster and with finer spatial resolution than FDM printers [23, 24]. These printers rely on photopolymerization to initiate the polymerization of a liquid into a solid. This is achieved by projecting a 2D pattern of light (digital light processing (DLP)) [25, 26] or by raster-scanning a beam of laser light (stereolithography (SLA)) [23, 27] into a photocrosslinkable liquid. Yet, despite their tremendous potential, formulations and techniques for printing hydrogels using light-based printers remain limited.

A primary issue limiting light-based 3D printing of hydrogels is the lack of a generalized approach to create objects with high resolution internal channels and voids in any desired orientation while minimizing channel occlusion (e.g. 'bleedthrough'). This entails controlled attenuation of the light [27, 28], which requires knowledge of how formulation composition and light exposure conditions affect polymerization conditions. Hydrogel structures containing submillimeter-scale voids that are constrained with axes oriented parallel or perpendicular to the light path (z-axis) have been reported [29, 30], and printed hydrogels containing submillimeter-scale channels with no orientation restrictions have recently been reported [28]; however, a generalizable approach for optimizing critical parameters such as layer resolution and light attenuation while mitigating channel occlusion is lacking. This is needed to optimize new photocrosslinkable liquid formulations (i.e. 'resins') for hydrogel printing and provide a framework for understanding the experimental limits of channel resolution. Complex internal channels are essential for a variety of bioengineering applications, but, without a clear optimization approach, the full potential of light-based printers cannot be met.

Here we present a generalizable method for light-based 3D printing of hydrogels containing well-defined, submillimeter-scale channels with any orientation. To characterize a new formulation, we begin by systematically measuring the single-layer cure depth as a function of light exposure and photoblocker concentration. Next, we determine the print conditions needed to adhere one layer to another by systematically varying single-layer cure depth and instrument-imposed layer thickness. Finally, we measure channel bleedthrough as a function of layer thickness, use this data to test bleedthrough models, and find that the effect of cumulative exposure contributes significantly to channel bleedthrough. To demonstrate the practicality of our approach, we print hydrogels containing spiral channels with centimeter-scale length and submillimeter-scale cross-section and establish liquid flow through these channels.

Background

In stereolithography (SLA)-based 3D printing, a solid object is built layer-by-layer from a liquid resin using a focused laser spot. Photopolymerization occurs at the laser focal point, which is raster-scanned within the *xy*-plane of the resin bath to create a single layer which adheres to the print head (figures 1(a), (b)). The print head is then moved upwards in the z-direction and the next layer is printed onto the previous layer. Polymerization typically occurs through free-radical transfer: a photoinitiator absorbs laser light to form a reactive species and initiates a reaction cascade by which low molecular weight monomers react to form high molecular weight polymers and eventually a crosslinked solid. The polymerization process terminates through free radical combination or when free radicals become topologically constrained [27]; thus, the reaction does not propagate through the entire bath after polymerization is initiated by the laser light.

As each successive layer is added to a printed object, the laser light needed to polymerize a new layer passes into previously printed layers (figure 1(a)). This condition is necessary for the adhesion of one layer to the next but can be problematic if the printed object is meant to contain voids or overhangs and bleedthrough occurs in these regions. Light is attenuated as it propagates into the resin, so the intensity decreases with penetration depth, z. At some depth, the light

becomes insufficient to induce polymerization; this is referred to as the cure depth, C_d, beyond which the resin remains liquid (figure 1(c)). For an object composed of multiple layers, the balance between necessary overlap and undesired curing can be determined by comparing two lengths: the layer thickness, ℓ_z, which is set by the incremental, vertical movement of the print head, and the cure depth, C_d, which is set by the composition of the resin and exposure conditions. Thus, when formulating a new resin, knowledge of C_d is critical.

A variety of photopolymerizable hydrogel formulations for use with 3D printing have been reported, including polyethylene glycol-diacrylate (PEG-DA) gels [20, 31], polyethylene glycol-diacrylamide (PEG-DAAm) gels [32], and Pluronic monocarboxylate-gelatin methacrylate (Plu-GelMA) composite gels [33, 34]; however, knowledge of how formulation variables affect printing parameters such as C_d is lacking. As a result, it is difficult to quantify and compare advances in the spatial resolution of light-based hydrogel printing. Additionally, most studies focus on digital light projection (DLP) systems or SLA printers that use ultraviolet light, and, to our knowledge, no studies involving SLA printers that make use of violet ($\lambda = 405$ nm) light have been reported. This may be important if living cells are incorporated into the liquid resin and exposed to laser light during the printing process as violet light is lower in energy than ultraviolet light, is not strongly absorbed by DNA [35], and has shown to be less cytotoxic for a variety of mammalian cells [36–39].

In this context, we focus on characterizing a photopolymerizable hydrogel resin formulation for use with violet laser light that can be used to generate hydrogels with high-resolution internal channels using components that are generally accepted as non-cytotoxic. Two primary components of any photopolymerizable formulation are a reactive monomer and a photoinitiator. For the hydrogel monomer, we choose PEG-DA to create PEG-based hydrogels, which are considered a benchmark for non-cytotoxic hydrogels [4, 40]. Mammalian cells do not adhere to PEG gels, so, for applications incorporating living cells, the gel would need to be functionalized [20, 31, 32]; however, for the purposes of this study, we use non-functionalized PEG. For the photoinitiator, we choose lithium phenyl-2,4,6-trimethylbenzoylphosphinate (LAP) [41, 42]. LAP is freely soluble in water, has been shown to be biologically inert [41], and absorbs light in the UV and low visible range with high efficiency. This formulation pair is well-established for a variety of non-3D printing hydrogel applications; however, when printing is attempted using a light-based 3D-printer (Formlabs, Form 1+), the polymerized gel layers are very thick. Thus, a third formulation component, one that strongly attenuates the laser light, is required: a photoblocker. This component is critical for achieving high-resolution printing with any light-based 3D printer (e.g. SLA or DLP). Several photoblockers including Quinolone Yellow [28] and Sudan I [43] have been reported for use in photopolymerizable hydrogel applications. Here we explore the use of chlorophyllin and tartrazine. Chlorophyllin is a hydrolyzed version of chlorophyll that is soluble in water and strongly absorbs blue-violet light (supplemental information, SI figure 1 is available online at stacks.iop.org/BPEX/5/025035/mmedia) [44]. Tartrazine is yellow azo dye commonly found in food coloring, with strong absorbance at 405 nm [45]. To our knowledge, this is the first reported use of both these compounds as photoblockers for photopolymerization applications.

Results & discussion

For the hydrogel formulations used here, light attenuation is dominated by the photoblocker. In the absence of photoblocker, the aqueous PEG-DA/LAP print formulation provides a cure depth on the order of centimeters (figure 2(a); $C_d \approx 1.85$ cm) for moderate exposures on a commercially available 3D SLA printer (see Methods). By comparison, under identical print conditions, the addition of chlorophyllin at a concentration of only 0.01 wt% results in a striking reduction in cure depth (figure 2(b); $C_d \approx 0.50$ mm). To quantify the capacity of chlorophyllin as a photoblocker, we systematically measure C_d as a function of light exposure and chlorophyllin concentration. We do this experimentally by removing the print head, printing a single layer, which adheres to the bottom surface of the resin tray, and measuring the thickness of that layer with optical coherence tomography (see Methods and SI figure 2). Light exposure is defined as the total integrated energy of laser light that passes through a given area. For an SLA printer, exposure is proportional to laser power and inversely proportional to the velocity at which the laser is scanned (see Methods). The exposure profile in z is expected to fall off exponentially as $E(z) = E_0 \exp(-z/D_p)$, where E_0 is the exposure at the bottom of the resin tray just as the laser light enters the resin ($z = 0$), and the penetration depth, D_p is the length scale that characterizes the exponential decay. Setting $z = C_d$, defining E at this depth as the critical exposure, E_c below which a gel does not form, and solving for C_d provides the following: $C_d = D_p \ln(E_0/E_c)$, as shown elsewhere [27, 41, 46]. Thus, plotting C_d as a function of E_0 on a linear-log scale should provide a straight line with a slope of D_p and an x-intercept corresponding to E_c, as has been shown extensively in the light-based 3D printing literature [27, 29].

We find that our data obtained with low to moderate exposure values are described well by the theoretical prediction. Plots of C_d versus E_0 for five different chlorophyllin concentrations, $c_b = 0.108$, 0.215, 0.430, 0.645, and 0.860 mg ml^{-1} are shown in figure 2(c), with fits to the solid symbols. As expected, the characteristic penetration depth, D_p, described by the slope of each fit, decreases with increasing

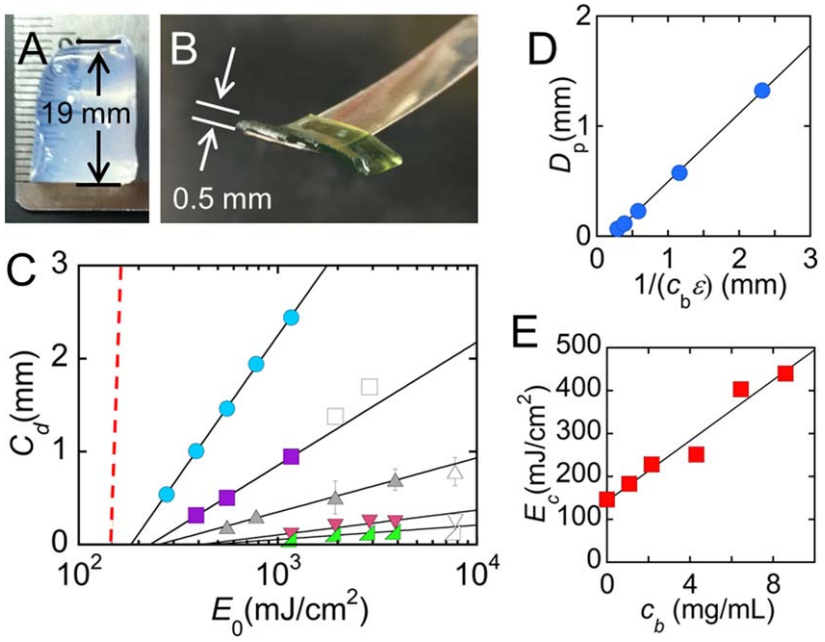

Figure 2. *Chlorophyllin as a photoblocker*. Photographs of PEG-DA hydrogel single layers printed (**A**) without photoblocker and (**B**) with 0.01 wt% chlorophyllin photoblocker using an SLA 3D printer with the same exposure conditions. Thickness of the gel represents the cure depth, C_d. (**C**) Single layer cure depth, C_d as a function of light exposure, E_0 for PEG-DA/LAP aqueous formulations with different chlorophyllin concentrations (c_b = 0.108 (●), 0.215 (■), 0.430 (▲), 0.645 (▼), 0.860 (right triangle) mg/ml). Lines are fits of solid symbols to $C_d = D_p \ln(E_0/E_c)$ (0.108 mg ml^{-1}, $R^2 = 0.999$; 0.215 mg ml^{-1}, $R^2 = 0.999$; 0.430 mg ml^{-1}, $R^2 = 0.996$; 0.645 mg ml^{-1}, $R^2 = 0.876$; 0.860 mg ml^{-1}, $R^2 = 0.920$). Open symbols not included in fit. Red, dashed line is fit to data for $c_b = 0$ mg/ml, which are out of scale ($C_d > 3$ mm) and thus not shown (see Methods). (**D**) Characteristic length scale associated with light attenuation, D_p as extracted from the slope of the fits in (C), and plotted as a function of $(c_b\varepsilon)^{-1}$ ($R^2 = 0.999$). (**E**) Critical exposure, E_c determined from the x-intercept of the fits in (C) and plotted as a function of c_b ($R^2 = 0.880$).

chlorophyllin concentration; that is, more chlorophyllin results in more attenuation. For very high exposure values, the data diverges slightly from the fit. For the three highest concentrations (c_b = 0.430, 0.645, and 0.860 mg ml^{-1}) the data at high exposure values demonstrates sub-logarithmic behavior. This has been reported previously for non-hydrogel resins, and has been attributed to the potential development of microscopic inclusions [27] such as bubbles or aggregates at high exposures, which result in scattering. The next lowest concentration (c_b = 0.215 mg ml^{-1}) exhibits super-logarithmic behavior at high exposures. This has been reported previously as well, and has been attributed to photobleaching and self-focusing [27]. These deviations are not relevant for most 3D printing applications as exposure values $E_0 \leqslant 10^3$ mJ cm^{-2} are typically used.

To better understand the dependence of D_p on c_b, we consider the Beer–Lambert Law, $A = \varepsilon L c_b$, which relates the absorbance of light, A, to the absorptivity coefficient ε, the path length traveled by light L, and concentration c_b. Absorbance is commonly defined as $A = \log_{10}(I_0/I(L))$, where I_0 is the intensity of the incident light and $I(L)$ is the intensity of the light after passing through a sample of thickness L. Absorbance can also be expressed in terms of exposure: $A = \log_{10}(E_0/E(L))$. Setting $E(L) = E(C_d)$, combining with the Beer–Lambert relationship, and solving for C_d provides $C_d = (1/\varepsilon c_b)\log_{10}(E_0/E_c)$. Combining this equation with the previously described equation for C_d yields $D_p = a/(\varepsilon c_b)$, where the coefficient a, the consequence of a change of base, should equal 0.4343. This provides a theoretical prediction of the relationship between D_p and c_b. To test this prediction, we plot D_p as a function of $1/(\varepsilon c_b)$, as shown in figure 2(d). The linearity of the resulting plot is striking, and the data fits well to the following form: $D_p = [a/(\varepsilon c_b)] - b$, where $a = 0.6208$ and $b = 0.1265$. While the physical origin of the difference in the slope, a, and the presence of an offset, b is unclear, the $1/c_b$ scaling above b captures the basic physics of photoblocker attenuation. Preliminary results with photoblockers such as tartrazine, fast green FCF, and sunset yellow show better agreement with our theoretical prediction, a topic which warrants further study.

The minimum exposure required for gel formation is defined as the critical exposure E_c and can be determined from the x-intercept for each curve in figure 2(c) as the cure depth goes to zero. We plot E_c as a function of c_b and find that E_c increases proportionally with c_b from a constant value at $c_b = 0$ (figure 2(e)). In free-radical photopolymerization reactions, the presence of oxygen, which is a known scavenger of free radicals, has been shown to increase E_c [27]. Thus, it is not surprising that chlorophyllin,

which is also known to react with free radicals, has a similar effect. The minimal increase in E_c due to chlorophyllin should not inhibit printing since the E_c values at the highest c_b are at least an order of magnitude below exposures easily achieved with available violet lasers on commercially available printers. However, the increase in E_c may become important when attempting to both maximize spatial resolution and minimize light exposure.

To move beyond single layers and print 3D objects containing internal voids, layer-layer adhesion must be ensured while minimizing bleedthrough. To find the optimal balance between these opposing factors, we design a test geometry: a hydrogel cube (dimensions: 6 mm × 6 mm × 6 mm) containing an internal, fully-enclosed rectangular channel with a square cross-section (dimensions: 1.5 mm × 1.5 mm ×3 mm; see SI figure 3). The enclosed channel design prevents the exchange of liquid between the channel and resin bath and thus represents conditions which will result in maximal channel bleedthrough, h_e such as a channel printed deep within a hydrogel where liquid exchange is limited. Intuition suggests that layer-layer adhesion will be achieved by meeting the condition $C_d \geqslant \ell_z$. To test this, we print the test geometry under varied conditions of ℓ_z and C_d. We vary ℓ_z over the range 6.25 μm $\leqslant \ell_z \leqslant$ 300 μm by controlling the gap between the underside of the printed object and inner surface of the resin tray, and vary C_d from 100 μm, 150 μm, and 200 μm by selecting E_0 from the working curves in figure 2(c). After printing, we evaluate each cube for layer-to-layer adherence and mechanical integrity using stereomicroscopy and classify the print as a success or failure.

For print conditions where $\ell_z > C_d$, a newly-cured layer should have insufficient thickness to bridge the gap between the bottom of the tray and the bottom surface of the previous printed layer. Thus, one would expect print failure due to non-adherence between layers. We find that near the $\ell_z = C_d$, boundary, layers still adhere to one another, but the object collapses and deforms as it is printed (figure 3(A), right: failure). As ℓ_z is increased, we eventually observe total failure; layers do not adhere to one another and remain dispersed in the resin bath (not shown). Surface irregularities are not used as a criterion for success-failure as successfully printed objects well within the $\ell_z < C_d$ region have rough surfaces (figure 3(B), left: success). This issue, which is common with light-based 3D printers, is easily resolved by including a high-exposure raster step around the boundary of each layer, creating a smooth outer surface. For layer-layer adhesion tests, this step was excluded.

Results for all printed objects are compiled as a plot of C_d versus ℓ_z in figure 3(b). Here, each data point represents an individually-printed cube, with green circles corresponding to successful prints and red squares corresponding to failed prints. The data falls into two regions, with successful prints at low ℓ_z,

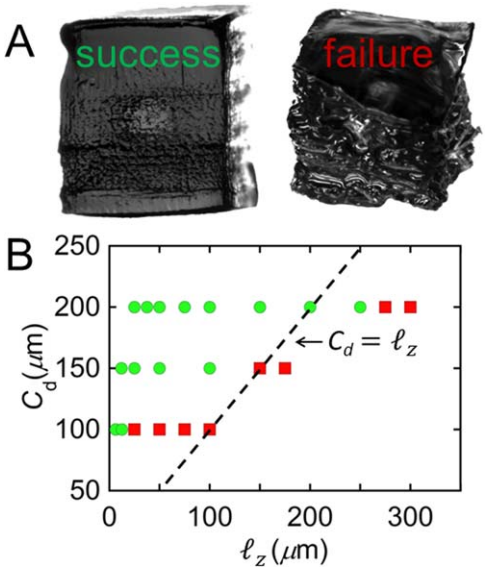

Figure 3. *Determining optimal layer-layer adhesion conditions for printing 3D objects.* (**A**) Stereomicroscopy images of hydrogel test cubes (outer dimensions: 6 mm × 6 mm ×6 mm) each printed under defined conditions (left: C_d =150 μm, ℓ_z = 25 μm; right: C_d = 150 μm, ℓ_z = 150 μm) then imaged and classified as a success or failure. The success-failure criterion was based on mechanical integrity and not surface irregularities, which are an aesthetic issue that is straightforward to address. (**B**) Plot of C_d versus ℓ_z generated from the classification of 22 individual cubes printed with c_b = 0.430 mg ml^{-1}. Prints that retain mechanical integrity are plotted as green circles and prints that do not retain integrity are plotted as red squares. Dashed line represents the expected success-failure boundary, $C_d = \ell_z$.

failed prints at high ℓ_z, and a distinct transition between success and failure. Successfully-printed objects subjected to tensile and shear stresses do not fail along layer-layer interfaces. This indicates that the adhesive yield stress is equal to or greater than the cohesive yield stress and that layer-layer adhesion is chemical in nature, rather than mechanical. This is not surprising, given that residual free radicals and unreacted monomers and oligomers remain in previously-printed layers [27] which could lead to reaction and interpenetration between gel layers.

To understand the success-failure transition, we superimpose the defining line at which we would expect layer-layer adhesion to fail: $C_d = \ell_z$. This line represents a boundary to the right of which one would expect objects to lose mechanical integrity. When we overlay this line onto our data, the agreement in the center of our data range ($C_d = \ell_z$ =150 m) is good; however, at low C_d, the ℓ_z value associated with the transition from success to failure occurs at a lower value than predicted, while at high C_d, the ℓ_z value associated with the transition from success to failure occurs at a greater value than predicted. The discrepancy between our data and the prediction can potentially be explained by several scenarios. First, the resin tray used to determine the working curves in figure 2(c) differs, by necessity, from the resin tray used to print 3D objects, and differences in tray thickness and material refractive index (see

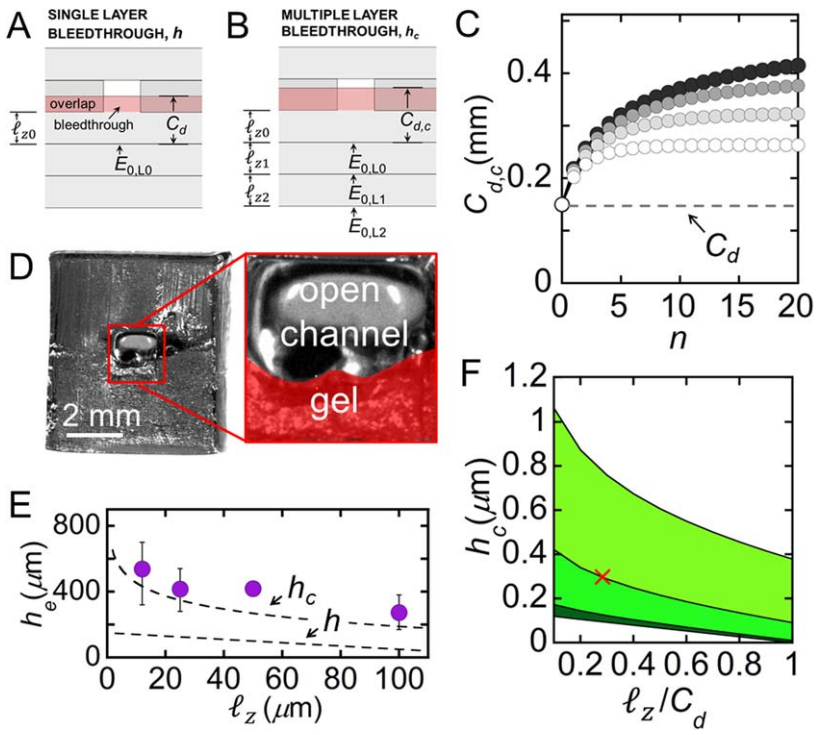

Figure 4. *Modeling and measuring channel bleedthrough.* (**A**) *Single-layer model:* the simplest scenario; bleedthrough into a void is just $h = C_d - \ell_z$. In this illustration (A), as well as (B) and (D), the laser is directed upwards along the z-axis (from bottom to top). (**B**) *Multiple-layer model*: the effect of repeated exposure results in a cumulative cure depth $C_{d,c}$ larger than C_d. (**C**) Calculated C_d, c as a function of n for $C_d = 0.15$ mm and (from bottom to top) $\ell_z = 12\ \mu$m, 25 μm, 50 μm, and 100 μm. (**D**) Image of a hydrogel cube containing an enclosed void space after being cut in half and an exposed face imaged with stereomicroscopy. Channel bleedthrough, h_e is quantified by measuring the extent of channel occlusion (see inset). (**E**) Plot of channel bleedthrough, h_e as a function of layer thickness ℓ_z, for $C_d = 0.15$ mm and $c_b = 0.430$ mg ml^{-1}. Measured bleedthrough is greater than predicted by the single-layer model (lower dashed line), and is in agreement with the multiple-layer model (upper dashed line). (**F**) Numerical calculations of h_c as a function of ℓ_z for $C_d = 132\ \mu$m over the range: 13.2 μm $\leqslant \ell_z \leqslant$ 132 μm for differing c_b plotted as a function of ℓ_z/C_d. From top to bottom, the bounding lines represent h_c values for $c_b = 0.215$ mg ml^{-1}, 0.430 mg ml^{-1}, and 0.860 mg ml^{-1}. The lowest bounding line represents $h = C_d - \ell_z$. The red mark represents print conditions for figures 5(b), (c).

Methods) could result in differences in light attenuation. Second, the gel-liquid boundary is likely not a sharp interface but rather a diffuse boundary, and it is not clear how thick this boundary is or how boundary thickness changes with C_d. Despite the lack of agreement, mapping print parameters in this manner provides a valuable and practical guide for choosing print coordinates.

For solid objects with no internal voids or overhangs, choice of print parameters should not significantly affect print quality as long as the parameters fall to the left of the success-fail transition. However, for objects containing internal voids, choice of print parameters will determine the amount of bleedthrough into the void space. To define the expected upper and lower limits of bleedthrough, we construct two models. In the lower limit, bleedthrough is described by considering only the contribution of the layer directly beneath a void. This is simply the difference between the cure depth and layer thickness: $h = C_d - \ell_z$ (figure 4(a)). In the upper limit, the contribution of multiple subsequent exposures must be considered. That is, when multiple layers are printed beneath a void, even if light is attenuated such that it is below the gelation threshold when it reaches the void, repeated exposure will have a cumulative effect (figure 4(b)). To model this effect, we define the cumulative incident exposure for a particular layer as $E_{0,c} = (\sum_{i=0}^{n} E_0 10^{-[\varepsilon c_b] i \ell_z})$, where n is the number of layers printed below a void. This summation of exposures is based on the assumption that the same resin volume is being repeatedly exposed and is not mixed in the channel or freely exchanged with the resin bath. The cumulative cure depth is then described as $C_{d,c} = D_p \ln(E_{0,c}/E_c)$ and the overlap is $h_c = C_{d,c} - \ell_z$. It is important to note that the cumulative cure depth, $C_{d,c}$ can be much larger than C_d. To demonstrate this, theoretical predictions for $C_{d,c}$ for $C_d = 150\ \mu$m and $\ell_z = 12\ \mu$m, 25 μm, 50 μm, and 100 μm are plotted as a function of n in figure 4(c). For the curves plotted here, $C_{d,c}$ approaches an asymptote, the value of which increases as ℓ_z decreases, and this asymptote in $C_{d,c}$ can be significantly larger than C_d. For example, for $C_d = 150\ \mu$m and $\ell_z = 100\ \mu$m, $C_{d,c} \approx 450\ \mu$m, three times larger than C_d.

To experimentally determine the extent to which cumulative exposure impacts bleedthrough, we select printed hydrogel cubes, each containing an internal, fully-enclosed rectangular channel with square cross-section, cut each cube in half, and image the channel

cross-section using stereomicroscopy (figure 4(d)). We do this for four cubes, all printed using C_d = 150 μm (c_b= 0.430 mg ml^{-1}), but with varying ℓ_z = 12.5 μm, 25 μm, 50 μm, and 100 μm. After measuring the average bleedthrough in the enclosed channel, h_e, find that h_e decreases with increasing ℓ_z, as expected (figure 4(e)). To compare our data with the minimum and maximum theoretical estimates for bleedthrough, we include these predictions as dashed lines and find that our measurements agree well with the cumulative model prediction (figure 4(e), upper line). This supports our hypothesis that the cumulative effect of repeated exposure must be considered and provides a theoretical framework for minimizing channel occlusion during printing.

To better understand the dependence of h_c on experimental parameters, we rearrange the expression for the cumulative model (see SI Text) to obtain: $h_c = h + D_p \ln(\sum_{i=0}^{n} 10^{-[\varepsilon c_b] i\ell_z})$. This form reveals that for fixed C_d and ℓ_z, h_c should decrease with increasing photoblocker concentration, and, in the limit where $c_b \to \infty$, $h_c \to h$. This can be understood by considering two formulations with different c_b. The solution with greater c_b will have a smaller D_p. Thus, to achieve the same C_d, E_0 for the more concentrated solution must be increased until the exposure curves cross over at the same z value ($z = C_d$). Importantly, beyond this crossover, $E(z)$ will decrease more precipitously for the more concentrated solution than the less concentrated solution. This means that cumulative exposure will decrease with increasing c_b for fixed C_d. To show this, we solve the expression above numerically for our chlorophyllin formulation. We choose C_d = 132 μm, calculate h_c as a function of ℓ_z over the range: 13.2 μm $\leqslant \ell_z \leqslant$ 132 μm for c_b = 0.215 mg ml^{-1}, 0.430 mg ml^{-1}, and 0.860 mg ml^{-1}, and plot h_c as a function of ℓ_z / C_d. Our numerical calculations confirm that h_c decreases with increasing c_b, as shown in figure 4(f). This provides a guide for choosing the c_b necessary to print channels of a given size with an acceptable degree of occlusion.

To show the value of this approach, we use our experimental finding to print hydrogels containing well-defined channels with centimeter-scale length, submillimeter-scale cross-section and varying orientation. We do this by choosing print conditions (C_d = 132 μm and ℓ_z = 37.5 μm) that lie within the success region in figure 3(b). With these conditions, and for c_b= 0.430 mg ml^{-1} and ℓ_z/C_d= 0.28, the estimated value of cumulative bleedthrough is $h_e \approx$ 200 μm (figure 4(f), red mark). A spiral channel geometry is chosen as a printing benchmark because the channel orientation varies continuously between vectors parallel and perpendicular to the light-path throughout the length of the channel, and print success is easily determined by observation of flow through the channel. An illustration of the print design is shown in figure 5(a), and liquid flow through the printed object is shown by the series of microscopy images in figure 5(b). In these images, air bubbles entrained in the liquid provide an indication of flow. The inscribed sectional diameter of the channel in the print file is 800 μm, and the inscribed sectional diameter of the channel in the printed object is approximately 600 μm. This is consistent with our bleedthrough prediction. To illustrate a slightly more complex channel design, we use the same conditions to print an object containing two separate, co-rotating spiral channels as shown in figure 5(c).

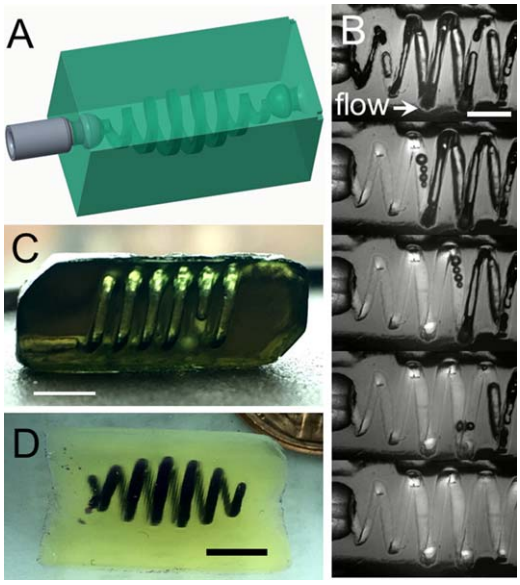

Figure 5. *Printed hydrogels with submillimeter channels.* (**A**) Illustration of a rectangular hydrogel containing a single spiral channel. (**B**) Microscopy image series depict flow of aerated liquid through a printed chlorophyllin hydrogel (design from (A)). Images are separated by Δt = 10 s. Scale bar corresponds to 2 mm. (**C**) Photograph of rectangular chlorophyllin-containing hydrogel containing two independent spiral channels. Two input/output channels are apparent on the ends of the rectangular cube; the remaining two are on the back of the cube. Water within the channels was expelled using compressed air for improved channel contrast, though some residual water remains, as apparent from the air-water meniscus in the second channel from the right. (**D**) Hydrogel cube containing a single spiral channel printed using tartrazine as photoblocker. Oil-based paint was injected into the channel for visualization purposes. Scale bars in (C) and (D) correspond to 5 mm.

Creating fully vascularized tissue constructs with *in vivo* complexity requires creating channels with varied orientations and cross-sectional diameters on the order of tens of microns. For the commercial printer used here, the smallest achievable channels will be limited by the beam waist of the focused laser spot q(140 μm, FWHM); thus, we expect channels on the order of several hundred microns to be our lower limit. Much smaller channels approaching the size of capillaries should be obtainable using DLP printers or custom SLA printers with more highly-focused light, where the *xy*-resolution is set by the diffraction limit. For these systems, our optimization approach should still be valid; to find the limit of channel resolution one would choose the highest possible photoblocker

concentration and move along the relevant h_c bounding line (figure 4(f)) by increasing ℓ_z or decreasing C_d until layers fail to adhere to one another. Upper limits for c_b and E_0 will be set by the saturation solubility of photoblocker and exposure at which printing parameters begin to deviate from the theoretical prediction. Lower limits for c_b and E_0 will be set by $c_b = 0$ mg/ml and E_c, respectively. In practice, parameter selection will likely depend on experimental constraints such as chemical and biological compatibility with photoblocker and sensitivity to light exposure.

This optimization approach can presumably be used to characterize any light-based 3D printing formulation. To illustrate this point, we replace chlorophyllin with tartrazine and measure C_d as a function of E_0 for $c_b = 0.15$, 0.30, and 0.45 mg ml^{-1}. We find the working curves to be well fit by the theoretical prediction $C_d = D_p \ln(E_0/E_c)$, the characteristic penetration depth to follow $D_p \sim 1/\varepsilon c_b$, and E_c to increase proportionally with c_b from a constant value at $c_b = 0$ (see SI figure 4). We then choose print conditions such that $C_d = \ell_z = 55$ μm, c_b= 0.75 mg ml^{-1} and print a single spiral geometry with equivalent dimensions to the chlorophyllin single spiral geometry as pictured in figure 5(d). By contrast to chlorophyllin, tartrazine does not bind to the gel; instead, when the hydrogel is placed in water, tartrazine diffuses out of the gel into the water. Thus, tartrazine provides an alternative photoblocker for creating transparent, nearly-colorless hydrogels with complex internal structures. This result supports the validity of our approach and provides a second photoblocker for use printing hydrogels with violet light.

Methods

Chemicals

Compounds were purchased from the following manufacturers and used directly without additional purification: polyethylene glycol diacrylate (PEG-DA, MW 700; Sigma Aldrich), lithium phenyl-2,4,6-trimethylbenzoylphosphinate (LAP, TCI Chemicals); sodium copper chlorophyllin (TCI Chemicals), 3-methacryloxypropyltrimethoxysilane (Amersham Biosciences), tartrazine (Fisher Scientific).

Resin formulation

Stock solutions containing 10 wt% PEG-DA and 0.1 wt% LAP dissolved in water were made in 200 ml batches. This concentration of PEG-DA was chosen to create gels with elastic moduli on the order of 10^3 Pa [47]. Each batch was prepared by combining 18 ml PEG-DA, 0.2 g LAP, and 182 ml water. Concentrated photoblocker solution was made by mixing 1 g chlorophyllin in 20 ml deionized water. Chlorophyllin concentrations were then set by adding microliter quantities of the concentrated chlorophyllin solution to milliliter quantities of the stock PEG-DA solution. The resulting dilution of PEG-DA and LAP was considered negligible. Chlorophyllin containing formulations were found to age (see SI figure 5); thus, for all experiments, solutions were used within 8 h of mixing.

SLA printer

The Form 1 + is a consumer SLA-based 3D printer manufactured by Formlabs (Somerville, MA) with the following specifications: laser wavelength $\lambda = 405$ nm (violet); maximum laser power, $P_{max} = 62$ mW, beam diameter $d = 0.16$ mm; z-axis minimum step increment, $z_d = 2.5$ μm; maximum build volume (OEM) $V_{max} = 12.5$ cm $\times$ 12.5 cm $\times$ 16.5 cm (4.9 $\times$ 4.9 $\times$ 6.5 in). *Modifications.* A print head was modeled to match the OEM head thickness reduced by 1 mm and printed in methacrylate on a Form 2 printer. A silanized, 1 mm glass microscopy slide was bonded to the bottom of the head with silicone caulk. A bottomless tray was bonded to the PDMS surface of the OEM resin tray, centered about the modified head, to reduce the volume necessary to fill the tank to a workable printing depth (see SI figure 6).

Print head silanation

To ensure adhesion of printed hydrogel to the print head, microscopy slides (Fisherbrand Colorfrost, 25 mm $\times$ 75 mm $\times$ 1 mm) were submerged in a 2.0 vol% solution of 3-trimethoxysilyl) propyl methacrylate in ethanol (Bind-Silane, GE Healthcare, 17-1330-01) for at least five minutes then held at 100°C for five minutes. This is a well-established protocol for coupling polymerizing hydrogel to a glass surface [16].

Print control

OpenFL, a version of Formlabs' proprietary slicing software with user adjustable curing profiles was used to control the 3D printer. All parameters relevant to exposure such as laser power P, laser velocity v, scanline spacing S, number of exposures per layer N, and layer thickness ℓ_z, were adjustable. The average incident exposure per layer per unit area was calculated as: $E_0 = \frac{PN}{Sv}$. This definition is made with the assumption that the sum of multiple repeated low power exposures is equivalent to a single higher power exposure, which has been shown to be valid for current SLA printers. For all prints, the scanline spacing was fixed at $S = 0.09$ mm for appropriate overlap of scanlines. Exposure was controlled by (1) increasing N, which effectively lengthened the duration of the exposure, (2) reducing v, which effectively lengthened the duration of the exposure, or (3) increasing P, which kept exposure duration constant.

Cure depth measurements

Single hydrogel layers did not adhere to the bottom of the PDMS-coated, OEM resin tray. Thus, to test single

layer cure depth, curing trays were made by gluing large (50 mm × 75 mm × 1 mm) silanized glass slides to the bottom of small bottomless Petri dishes (35 mm inner diameter) using silicone caulk. A clear cast acrylic plate (McMaster Carr, thickness, $h = 4.5$ mm) was laser cut to replace the OEM resin tray and fit into the resin tray slot (17.3 cm × 19.3 cm) of the printer. In the center of the acrylic, a hole was made to hold a curing tray. A basic working profile, which produced gels of acceptable quality was developed as a baseline for subsequent testing of cure depth. Beginning with the baseline profile, alternate profiles of varying exposures were added by increasing the number of exposures per layer N while keeping all other variables constant. For each measurement, the print head was removed and a single layer printed. The uncured liquid resin remaining in the cup was then discarded, the cup gently rinsed with water, and the gel thickness was measured with optical coherence tomography. Strong adherence of hydrogel layers to the glass-bottom resin tray precluded its use for printing multilayered objects. Differences between the OEM tray and custom, single-layer curing trays may lead to discrepancies between theory and experiment (figure 3(b)). For example, the OEM tray is composed of two layers: a 6.5 mm thick layer of PMMA (refractive index, $n = 1.49$) covered with a 1.5 mm thick layer of PDMS ($n = 1.40$), and the custom tray is composed of one layer of 1.0 mm thick layer of glass ($n = 1.52$).

OCT measurements

Gel layer thickness measurements were made using an optical coherence tomography machine (Leica Microsystems, Envisu 4310). A rectangular volume capture with two A-scans per pixel, were scanned over a 1 mm × 4 mm area. For samples thicker than 1 mm, a 3 mm × 3 mm area was scanned. The average gel thickness, as well as the upper and lower limits in thickness, were determined by analyzing individual B-scans.

Absorbance measurements

Measurements were performed using a plate reader (Biotek Synergy H1 Hybrid Reader). To hold the samples, a custom-built well plate was printed on the Form 2 printer. Six 25 mm diameter wells were positioned concentric to the equivalent positions of the B2, B6, B10, F2, F6, and F10 wells of a standard 96 well plate. Thin concentric lips were modeled at the bottom of the six holes to retain a 25 mm coverslip. For each sample, a small volume of liquid resin ($V = 130$ μl) was sandwiched between two round coverslips (Thomas Scientific, 25 Cir-No. 1) separated by an annular-shaped spacer (McMaster Carr, 90214A438; thickness, $h = 0.5 \pm 0.05$ mm, outer diameter, $d_o = 22$ mm; inner diameter, $d_i = 16$ mm) and loaded into each of the 6 wells. One well was reserved for water as a blank. To determine if the molar extinction coefficient of the resin changed with exposure time, a custom-built UV lamp was constructed to expose samples to spatially-uniform light, similar in wavelength to the Form1 + laser. The UV lamp was constructed using 13 individual LEDS (Mouser.com, EAUVA35352IJ8, 400 nm $\leqslant \lambda \leqslant$ 410 nm), mounted in parallel to each other, distributed evenly across a six inch square, copper clad, photo-etched circuit board. A 2.7 Ω resistor (Mouser.com, 279-SMW32R7JT) was mounted in series with each LED. A 5 V, 10 amp peak power supply was used to power the LEDs. The emitter array was mounted into a 20 cm^3 cardboard box with the bottom removed and a portion of the top cut out to receive the emitter. The current demand was then measured with all LEDs installed. Average current through each LED was taken as total current divided by the number of LEDs. With LED power emission plotted against current on the EAUVA35352IJ8 datasheet, power of each LED could be determined, summed amongst all LED's and divided by the box cross sectional area to determine power per unit area. Thus, exposure of any sample placed under the box could be controlled by duration of exposure. A series of varying exposure times for various photoblocker concentrations were then conducted to determine molar extinction coefficient of the photoblocker at various exposures.

Conclusion

Here, we present a systematic approach for structuring hydrogels containing well-defined microchannels using light-based 3D printing methods. The components used in the formulation are nontoxic, so the printed gels could potentially be used for applications involving living cells. In addition, the formulation composition could easily be modified to alter the physical and chemical properties of the gel, for example, through the addition of multifunctional crosslinkers or by chemical modification of the monomer. High print resolution is enabled by the incorporation of water-soluble photoblockers, which strongly absorb violet light; chlorophyllin and tartrazine are used here, but other water-soluble compounds that absorb violet light could be used. Our measurements of channel bleedthrough reveal that cumulative exposure contributes to undesired channel occlusion and must be incorporated into future models of channel bleedthrough. Finally, our experimental quantification of cure depth reveals a relationship between characteristic penetration depth, photoblocker concentration, and photoblocker absorptivity coefficient, which, to our knowledge, has not been reported and could provide an approach for rapidly quantifying new formulations.

Author contributions

Conceptualization: A D B and J N W; Methodology: A D B, R A, M O, and J N W; Investigation: A D B, R A, M O, R J O, T B L, and D W; Writing—Original

Draft: A D B, R A, and J N W; Writing, Review & Editing: A D B, R A, M O, R J O, T B L, and J N W; Funding Acquisition, Resources, and Supervision: J N W

Funding

This work was supported by the National Science Foundation (DMR-1455247, CBET-1626604, and OIA-1736255).

ORCID iDs

Reha Abbasi https://orcid.org/0000-0001-6240-2097
Thomas B LeFevre https://orcid.org/0000-0002-1340-9521
James N Wilking https://orcid.org/0000-0002-7255-7209

References

[1] Drury J L and Mooney D J 2003 *Biomaterials* **24** 4337–51
[2] Peppas N A, Bures P, Leobandung W and Ichikawa H 2000 *European Journal of Pharmaceutics and Biopharmaceutics* **50** 27–46
[3] Qiu Y and Park K 2001 *Adv. Drug. Deliv. Rev.* **53** 321–39
[4] Zhu J M 2010 *Biomaterials* **31** 4639–56
[5] Bowman C N and Kloxin C J 2008 *AIChE J.* **54** 2775–95
[6] Zhu W *et al* 2015 *Adv. Mater.* **27** 4411–17
[7] Slaughter B V, Khurshid S S, Fisher O Z, Khademhosseini A and Peppas N A 2009 *Adv. Mater.* **21** 3307–29
[8] Bae M, Divan R, Suthar K J, Mancini D C and Gemeinhart R A 2010 *J Vac Sci Technol B Microelectron Nanometer Struct Process Meas Phenom* **28** C6P24–26P29
[9] Qu X, Gou M, Zaidan J, Zhang K and Chen S 2014 *Nanomedicine (Lond)* **9** 2437–9
[10] Waheed S, Cabot J M, Macdonald N P, Lewis T, Guijt R M, Paull B and Breadmore M C 2016 *Lab Chip* **16** 1993–2013
[11] Floren M, Migliaresi C and Motta A 2016 *J Funct Biomater* **7**
[12] Billiet T, Vandenhaute M, Schelfhout J, Van Vlierberghe S and Dubruel P 2012 *Biomaterials* **33** 6020–41
[13] Ma X *et al Proc Natl Acad Sci U S A* 2016 **113** 2206–11
[14] Liu V A and Bhatia S N 2002 *Biomed. Microdevices* **4** 257–66
[15] El-Sherbiny I M and Yacoub M H 2013 *Glob Cardiol Sci Pract* **2013** 316–42
[16] Raman R, Bhaduri B, Mir M, Shkumatov A, Lee M K, Popescu G, Kong H and Bashir R 2016 *Adv Healthc Mater* **5** 610–9
[17] Ling Y, Rubin J, Deng Y, Huang C, Demirci U, Karp J M and Khademhosseini A 2007 *Lab Chip* **7** 756–62
[18] Ziaie B, Baldi A, Lei M, Gu Y and Siegel R A 2004 *Adv. Drug. Deliv. Rev.* **56** 145–72
[19] Slaughter B V, Khurshid S S, Fisher O Z, Khademhosseini A and Peppas N A 2009 *Advanced materials (Deerfield Beach, Fla.)* **21** 3307–29
[20] Warner J, Soman P, Zhu W, Tom M and Chen S 2016 *ACS Biomaterials Science & Engineering* **2** 1763–70
[21] Do A V, Khorsand B, Geary S M and Salem A K 2015 *Adv Healthc Mater* **4** 1742–62
[22] Shi W, He R and Liu Y 2015 *European Journal of BioMedical Research* **1** 3–8
[23] Melchels F P, Feijen J and Grijpma D W 2010 *Biomaterials* **31** 6121–30
[24] Tumbleston J R *et al* 2015 *Science* **347** 1349
[25] Zhang A P, Qu X, Soman P, Hribar K C, Lee J W, Chen S and He S 2012 *Adv. Mater.* **24** 4266–70
[26] Gauvin R, Chen Y C, Lee J W, Soman P, Zorlutuna P, Nichol J W, Bae H, Chen S and Khademhosseini A 2012 *Biomaterials* **33** 3824–34
[27] Jacobs P F 1992 *Rapid Prototyping & Manufacturing: Fundamentals of StereoLithography*
[28] Zhang R and Larsen N B 2017 *Lab Chip* **17** 4273–82
[29] Arcaute K, Mann B K and Wicker R B 2006 *Ann. Biomed. Eng.* **34** 1429–41
[30] Lu Y, Mapili G, Suhali G, Chen S and Roy K 2006 *Journal of Biomedical Materials Research. Part A* **77** 396–405
[31] Chan V, Zorlutuna P, Jeong J H, Kong H and Bashir R 2010 *Lab Chip* **10** 2062–70
[32] Stevens K R, Miller J S, Blakely B L, Chen C S and Bhotia S N 2015 *Journal of Biomedical Materials Research Part A* **103** 3331–8
[33] Suntornnond R, Tan E Y S, An J and Chua C K 2017 *Sci Rep-Uk* **7** 16902
[34] Seo H, Heo S G, Lee H and Yoon H 2017 *RSC Adv.* **7** 28684–8
[35] Sambrook J 2001 *Molecular Cloning: a Laboratory Manual* 3rd edn (Cold Spring Harbor, NY: Cold Spring Harbor Laboratory Press)
[36] Jones C A, Huberman E, Cunningham M L and Peak M J 1987 *Radiat. Res.* **110** 244–54
[37] Wells R L and Han A 1984 *Mutation Research/Fundamental and Molecular Mechanisms of Mutagenesis* **129** 251–8
[38] Tyrrellw R M, Werfellim P and Moraer E C 1984 *Photochemistry and Photobiology* **39** 183–9
[39] Andley U P, Lewis R M, Reddan J R and Kochevar I E 1994 *Investigative Ophthalmology & Visual Science* **35** 367–73
[40] Browning M B, Cereceres S N, Luong P T and Cosgriff-Hernandez E M 2014 *J. Biomed. Mater. Res.* A **102** 4244–51
[41] Fairbanks B D, Schwartz M P, Bowman C N and Anseth K S 2009 *Biomaterials* **30** 6702–7
[42] Majiama T and Schnabel W 1991 *Makromol. Chem.* **192** 2307–15
[43] Han D, Lu Z, Chester S A and Lee H 2018 *Sci Rep-Uk* **8** 1963
[44] Oster G, Broyde S B and Bellin J S 1964 *J. Am. Chem. Soc.* **86** 1309–13
[45] Sikorski Z *et al* 2008 *Food Colorants* (Boca Raton: CRC Press)
[46] Miller G A, Gou L, Narayanan V and Scranton A B 2001 *Journal of Polymer Science Part A: Polymer Chemistry* **40** 793–808
[47] Rubinstein M C and Colby R H 2003 *Polymer Physics* (Oxford: Oxford University Press)